

# Octa- and Tetradecanuclear Mixed-Valent Vanadium(III/IV) Malates with Triazoles: Gas Adsorptions, Chiral Interface Recognition, and In Situ Decarboxylation

Zhen-Lang Xie and Zhao-Hui Zhou\*



Cite This: ACS Appl. Mater. Interfaces 2023, 15, 35710–35719



Read Online

ACCESS |

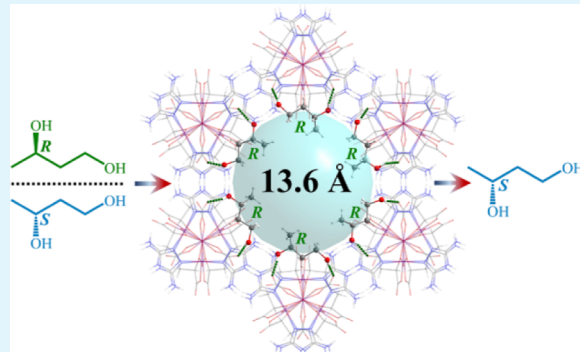
Metrics & More

Article Recommendations

Supporting Information

**ABSTRACT:** Spontaneous resolution has been found for a pair of cage-like octanuclear mixed-valent vanadium(III/IV) malate enantiomers  $[\Delta\text{-V}^{\text{III}}_4\text{V}^{\text{IV}}_4\text{O}_5(\text{R-mal})_6(\text{Hdatrz})_6]\cdot44.5\text{H}_2\text{O}$  ( $\Delta_{\text{R}}\text{-1}$ ) and  $[\Lambda\text{-V}^{\text{III}}_4\text{V}^{\text{IV}}_4\text{O}_5(\text{S-mal})_6(\text{Hdatrz})_6]\cdot38.5\text{H}_2\text{O}$  ( $\Lambda_{\text{S}}\text{-1}$ , H<sub>3</sub>mal = malic acid; Hdatrz = 3,5-diamino-1,2,4-triazole). Their racemic reduced product K<sub>7</sub>[V<sup>III</sup><sub>3</sub>V<sup>IV</sup><sub>3</sub>O<sub>5</sub>(R,S-mal)<sub>6</sub>(trz)<sub>6</sub>]·17H<sub>2</sub>O (2) and tetradecanuclear species K<sub>11</sub>[V<sup>III</sup><sub>3</sub>V<sup>IV</sup><sub>11</sub>O<sub>11</sub>(R,S-mal)<sub>12</sub>(atrz)<sub>6</sub>]·45.5H<sub>2</sub>O (3) (Htrz = 1,2,3-triazole, Hatrz = 3-amino-1,2,4-triazole) have also been obtained. In situ decarboxylation happens for 3-amino-1,2,4-triazole-5-carboxylic acid (H<sub>2</sub>atrzc) to yield 3-amino-1,2,4-triazole under hydrothermal conditions. Both **1** and **2** show an interesting bicapped-triangular-prismatic {V<sub>8</sub>O<sub>5</sub>(mal)<sub>6</sub>} building block, which further decorates symmetrically with three [V<sup>IV</sup><sub>2</sub>O<sub>2</sub>(R,S-mal)<sub>2</sub>]<sup>2-</sup> units to construct a pinwheel-like {V<sub>14</sub>} cluster, **3**. Bond valence calculation sum (BVS) analyses manifest that the oxidation states of bicapped V atoms are +3 in **1**–**3**, while the other V atoms in the {V<sub>6</sub>O<sub>5</sub>} core are ambiguous between +3 and +4 states with strong electron delocalization. Intriguingly, the triple helical chains in **1** associate in parallel to generate an amine-functionalized chiral polyoxovanadate (POV)-based supramolecular open-framework. The diameter of the interior channel is 13.6 Å, showing preferential adsorption of CO<sub>2</sub> over gases N<sub>2</sub>, H<sub>2</sub>, and CH<sub>4</sub>. Importantly, homochiral framework  $\Delta_{\text{R}}\text{-1}$  is capable of performing chiral interface recognition for R-1,3-butanediol (R-BDO) through host–guest interactions, as confirmed by the structural analysis of the host–guest complex  $\Delta_{\text{R}}\text{-1}\cdot\text{3(R-BDO)}$ . There are six R-BDO molecules in the channel of  $\Delta_{\text{R}}\text{-1}$ .

**KEYWORDS:** spontaneous resolution, chiral interface recognition, R-1,3-butanediol, gas adsorption, decarboxylation



## INTRODUCTION

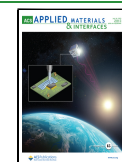
Chirality exists in nature ubiquitously at various hierarchical levels from subatomic to galactic scales.<sup>1–4</sup> Arguably, the most complex metallocluster identified to date in biological systems, like the caged FeV-cofactor (FeV-co), is a classic example of a high-nuclearity chiral metal-sulfur cluster. It acts as the active site for substrate binding and reduction in V-nitrogenase, whose structure has been elucidated as VFe<sub>7</sub>S<sub>8</sub>C(CO<sub>3</sub>)(R-homocit)(Hhis)(cys) (H<sub>4</sub>homocit = homocitric acid, cys = cysteine, Hhis = histidine).<sup>5–7</sup> It seems R-homocitrate chelates to metal vanadium(III) atom bidentately via  $\alpha$ -hydroxy and  $\alpha$ -carboxy groups, making an inorganic core of FeV-co asymmetric.<sup>8,9</sup> The environments around the inorganic core are also asymmetric by virtue of the protein backbones and the hydrogen bonds to the core. Although the absolute configuration of homocitrate can adopt *R* or *S* and the vanadium center can be  $\Delta$  or  $\Lambda$ , we can find only one absolute configuration  $\Delta_{\text{R}}$  in the five FeV-cofactors of FeV-proteins deposited in the Protein Data Bank (PDB entries: 5N6Y, 6FEA, 7ADY, 7ADR, and 7AIZ), as shown in Figure 1.<sup>5,10–12</sup> More recently, a V-nitrogenase variant VnfDGK<sup>Cit</sup> containing a

citrate-substituted FeV-co demonstrated a nearly twofold increase of the molar ratio NH<sub>3</sub>/H<sub>2</sub> from N<sub>2</sub> reduction compared to its wild-type counterpart.<sup>13</sup> Thus, the organic acidic component of FeV-co can be modified by homocitrate homologues for improved nitrogen fixation. Studies of chemical syntheses of FeV-co analogues could help to gain insight into the relationships between the structures and functions of cofactors. Previously, we reported a racemic heterometallic iron–vanadium malate cluster.<sup>14</sup> Here, we successfully construct a pair of enantiomeric mixed-valent vanadium(III/IV) model clusters  $[\Delta\text{-V}^{\text{III}}_4\text{V}^{\text{IV}}_4\text{O}_5(\text{R-mal})_6(\text{Hdatrz})_6]\cdot44.5\text{H}_2\text{O}$  ( $\Delta_{\text{R}}\text{-1}$ ) and  $[\Lambda\text{-V}^{\text{III}}_4\text{V}^{\text{IV}}_4\text{O}_5(\text{S-mal})_6(\text{Hdatrz})_6]\cdot38.5\text{H}_2\text{O}$  ( $\Lambda_{\text{S}}\text{-1}$ ). Moreover, their racemic

Received: May 6, 2023

Accepted: June 30, 2023

Published: July 12, 2023



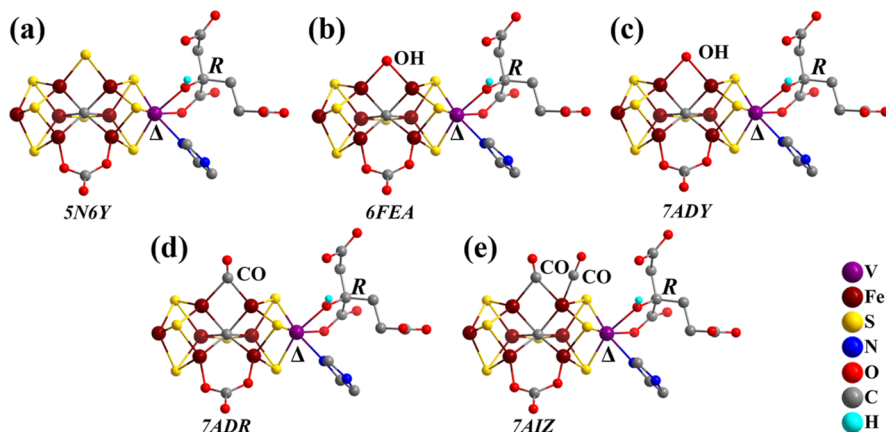
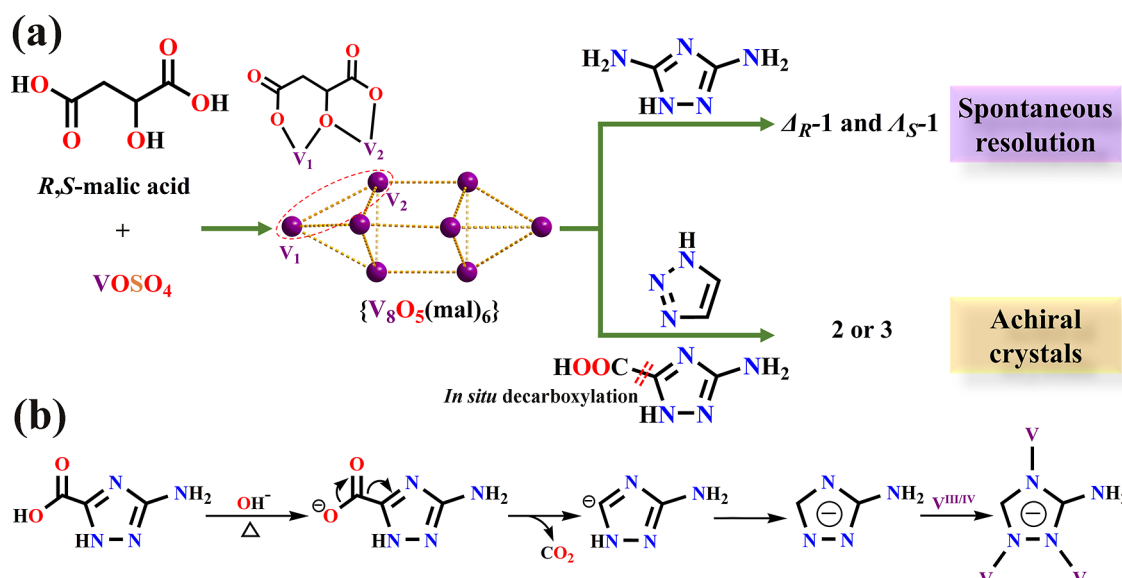


**Figure 1.** (a–e) Assignments of the absolute configurations in the five FeV-cofactors of FeV-proteins deposited in Protein Data Bank.<sup>5,10–12</sup>

**Scheme 1.** (a) Illustration of the Crystallization Process for 1–3 and (b) Possible Mechanism of Decarboxylation for the H<sub>2</sub>atrzc Ligand



complexes  $K_7[V^{III}_5V^{IV}_3O_5(R,S\text{-mal})_6(\text{trz})_6] \cdot 17H_2O$  (**2**) and  $K_{11}[V^{III}_3V^{IV}_{11}O_{11}(R,S\text{-mal})_{12}(\text{atrz})_6] \cdot 45.5H_2O$  (**3**) are also obtained by the self-assembly of racemic malic acid with VOSO<sub>4</sub> as well as achiral triazoles, where an interesting in situ decarboxylation reaction occurs in the formation of 3-amino-1,2,4-triazole. All of them are constructed from a bicapped-triangular-prismatic  $\{V_8O_5(\text{mal})_6\}$  building block. As expected, the absolute configuration  $\Delta_R$  and local chelation environment in  $\Delta_R\text{-}1$  show a little similarity with those of FeV-cofactors.

On the other hand, since the spontaneous resolution of sodium ammonium tartrates was first discovered and separated mechanically by Pasteur in 1848,<sup>15</sup> spontaneous resolution upon crystallization becomes an effective approach to obtain chiral metal clusters. Nevertheless, only 5–10% of racemates can undergo spontaneous resolution, while more than 90% of them crystallize as racemic compounds. In general, supramolecular interactions, such as hydrogen bonding and  $\pi\cdots\pi$  stacking interactions, are known to be of selective and directional nature and can serve as an efficient transfer of stereochemical information between adjacent homochiral molecules, playing a significant role in the process of spontaneous resolution.<sup>16</sup> Of particular interest is the

spontaneous resolution of the enantiomers in **1** upon crystallization, which undergoes self-assembly to generate homochiral supramolecular helices via intermolecular hydrogen bonding interactions. The triple helical chains in **1** associate in parallel to generate amine-functionalized chiral POV-based supramolecular open-frameworks with nanoscale channels. Moreover, benefiting from the tunable structure and high porosity, porous materials are attractive in the fields of gas capture and molecular detection.<sup>17,18</sup> Thus, gas adsorption properties and chiral interface recognition of **1** for small molecules are further investigated.

## RESULTS AND DISCUSSION

**Syntheses.** Octanuclear vanadium(III/IV) clusters **1**, **2**, and pinwheel-like  $\{V_{14}\}$ -cluster **3** were self-assembled by utilizing racemic malic acid and VOSO<sub>4</sub> under hydrothermal conditions. The products were obtained only in the limited pH ranges of 4–5. It is noteworthy that VO<sup>2+</sup> cations were reduced to low-valent V<sup>III</sup> precursors during hydrothermal treatment, which coupled to form mixed-valent V<sup>III/IV</sup> species. Spontaneous resolution of enantiomers  $\Delta_R\text{-}1$  and  $\Delta_S\text{-}1$  was discovered upon crystallization with 3,5-diamino-1,2,4-triazole

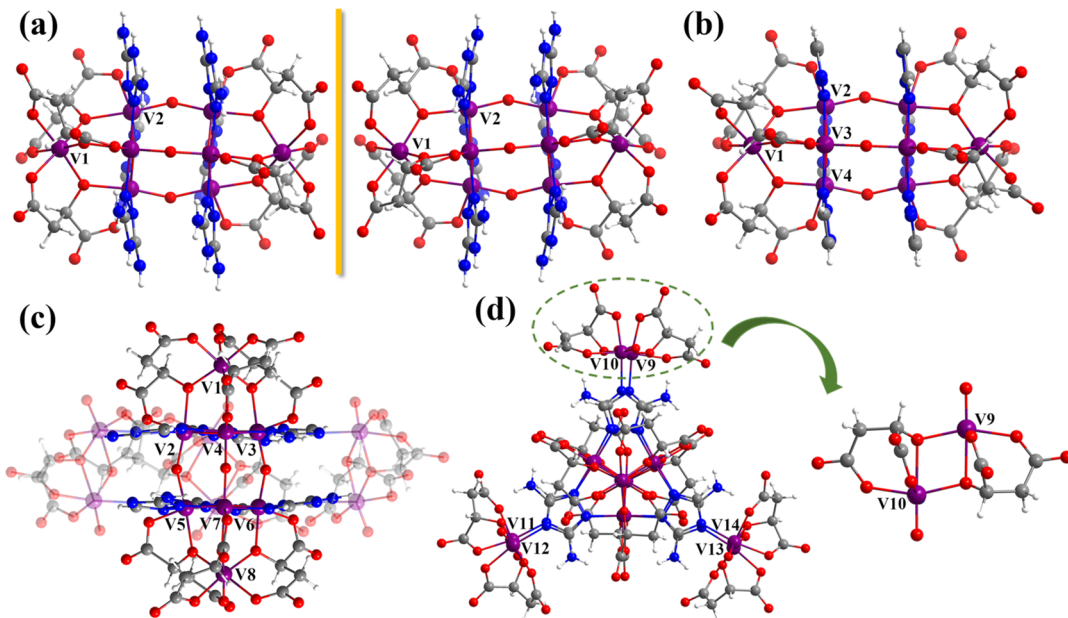


**Figure 2.** Perspective views of (a) enantiomers  $[V^{III}4V^{IV}4O_5(R\text{-mal})_6(\text{Hdatrz})_6] \cdot 44.5\text{H}_2\text{O}$  ( $\Delta_R\text{-1}$ , left) and  $[V^{III}4V^{IV}4O_5(S\text{-mal})_6(\text{Hdatrz})_6] \cdot 38.5\text{H}_2\text{O}$  ( $\Delta_S\text{-1}$ , right), (b)  $[V^{III}5V^{IV}3O_5(R,S\text{-mal})_6(\text{trz})_6]^{7-}$  (2), (c)  $[V^{III}3V^{IV}5O_5(R,S\text{-mal})_6(\text{atrz})_6]^{5-}$  fragment (3A, light area) and (d)  $[V^{IV}2O_2(R,S\text{-mal})_2]^{2-}$  unit (3B, right).

(Hdatrz) as an auxiliary ligand in Scheme 1. When we use 1,2,3-triazole (Htrz) or 3-amino-1,2,4-triazole-5-carboxylic acid ( $\text{H}_2\text{atrzc}$ ) as auxiliary ligands, only racemic complexes 2 and 3 were obtained. Unexpectedly,  $\text{H}_2\text{atrzc}$  suffered in situ decarboxylation to yield 3-amino-1,2,4-triazole (Hatrz) under hydrothermal conditions. Notably, decarboxylation did not happen in the absence of  $\text{VOSO}_4$ , suggesting that the V ion plays a catalytic role in the decarboxylation process. Other decarboxylations catalyzed by  $\text{Zn}^{2+}$  or  $\text{Cu}^{2+}$  cations have also been reported.<sup>19,20</sup> Upon the addition of base, it is proposed that the H atom in the carboxylic acid group was initially deprotonated, which gave rise to a zwitterion transition state at high temperatures.<sup>21</sup> The Hatrz<sup>-</sup> ligand further loses its carboxy group through cleavage of the C–C bond and release of the  $\text{CO}_2$  molecule.<sup>22</sup> Multiple attempts to obtain sample 3 directly with 3-amino-1,2,4-triazole under the same conditions were unsuccessful, suggesting that in situ ligand synthesis has a crucial effect.

**Structural Analyses.** X-ray structural analyses revealed that enantiomers  $\Delta_R\text{-1}$  and  $\Delta_S\text{-1}$  crystallize in the hexagonal chiral space group  $P6_{3}22$  with Flack parameter values of 0.063(2) and 0.022(8), respectively, corroborating the absolute configurations in the crystals, whereas 2 and 3 belong to the monoclinic and triclinic centrosymmetric space groups  $C2/c$  and  $P\bar{1}$ , respectively. Both  $\Delta_R\text{-1}$  and  $\Delta_S\text{-1}$  are neutral vanadium clusters, whereas the polyanionic structures 2 and 3 are further charge-balanced by potassium counterions. Pinwheel-like  $\{V_{14}\}$ -cluster 3 can be described as three  $[V^{IV}2O_2(R,S\text{-mal})_2]^{2-}$  units (denoted as 3B) symmetrically connected to the  $[V^{III}3V^{IV}5O_5(R,S\text{-mal})_6(\text{atrz})_6]^{5-}$  fragment (denoted as 3A) through six 3-amino-1,2,4-triazoles at the 4-position N atoms. As portrayed in Figures 2 and S1, octanuclear vanadium clusters 1–3A are constructed from bicapped-triangular-prismatic  $\{V_8O_5(\text{mal})_6\}$  building blocks decorated with different derivatives of triazoles. The  $\{V_8O_5(\text{mal})_6\}$  building block consists of a  $\{V^{III/IV}6O_5\}$  core combined with two end-capped  $V^{III}$  ions via  $\alpha$ -alkoxy groups of

six tridentate malates. In the  $\{V^{III/IV}6O_5\}$  core, six  $V^{III/IV}$  ions lie at the vertices forming a triangular prism, in which three  $\mu_2\text{-O}$  and two  $\mu_3\text{-O}$  atoms locate at the lateral edges and the triangular bases, respectively. All V ions in 1, 2, and 3A satisfy six coordination and adopt distorted octahedral configurations. The capped  $V^{III}$  cations (V1 for 1 and 2 and V1 and V8 for 3A) are defined by six oxygen atoms derived from  $\alpha$ -alkoxy and  $\beta$ -carboxy groups of three malates, while  $V^{III/IV}$  cations (V2 for 1, V2–V4 for 2, V2–V7 for 3A) are completed by four O atoms from  $\alpha$ -alkoxy,  $\alpha$ -carboxy,  $\mu_2\text{-O}$  and  $\mu_3\text{-O}$  groups and two N atoms from two adjacent triazole ligands, respectively. As demonstrated in Scheme 1 and Figure 3a,c, each malate ligand adopts a  $\mu_2\text{-}\eta^1\text{:}\eta^1\text{-}\eta^2$  coordination mode. The five-membered chelation in 1–3 is typical via  $\alpha$ -alkoxy and  $\alpha$ -carboxy groups, which is different from our early suggestion of  $\alpha$ -hydroxy and  $\alpha$ -carboxy groups in homocitrate of FeV-co.<sup>8</sup>

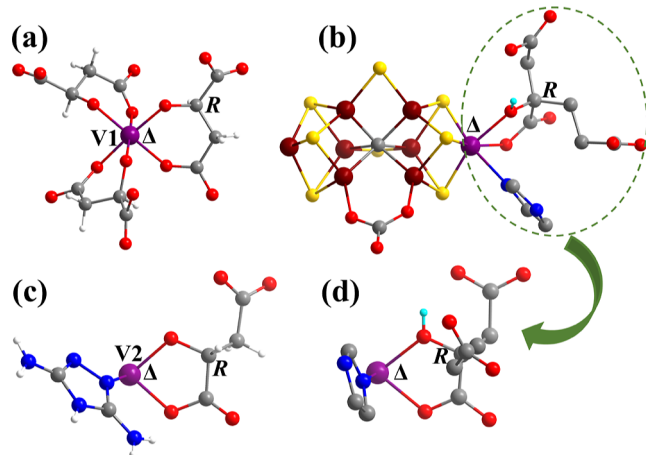


**Figure 3.** Absolute configurations of V(III) centers in (a)  $\Delta_R\text{-1}$  and (b) FeV-co (SN6Y). Comparison of local chelated structure in (c)  $\Delta_R\text{-1}$  and (d) FeV-cofector.

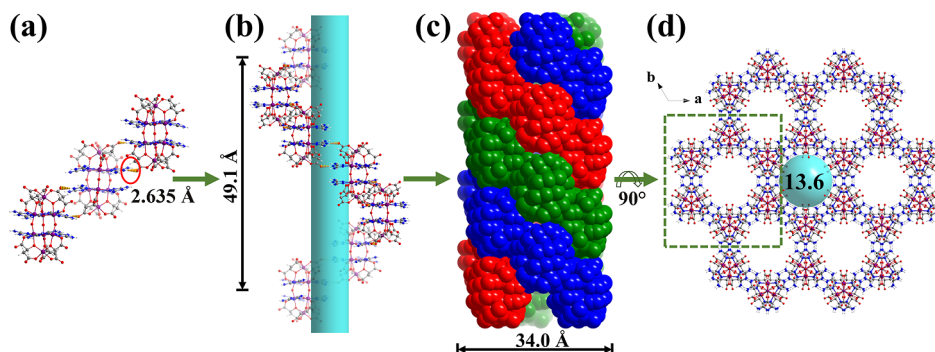


**Figure 4.** Formation of a helical structure. (a) Adjacent  $\Delta_{R-1}$  connected by intermolecular hydrogen bonds ( $N-H\cdots O$ ), forming helical building blocks. (b) Left-handed helical chain in  $\Delta_{R-1}$ . (c) Space-filling view of triple helical chains associate in parallel to generate a nanotube in  $\Delta_{R-1}$ , with each main strand colored separately for identification. (d) Channels in  $R-1$  viewed along the  $c$ -axis (unit: Å).

The other bidentate chelation with a six-membered ring has also been found in the two  $\beta$ -carboxy groups of malates. The absolute configuration of the V1(III) center in  $\Delta_{R-1}$  is assigned as  $\Delta$ , analogous to that in FeV-co in Figure 3b–d.

**3B** consists of a dimeric rhombic  $\{V^{IV}O_2\}$  core to which two triply deprotonated malates are attached in a  $\mu_2\eta^1:\eta^1:\eta^2$  fashion. Unlike the previously reported dimeric vanadium malates  $K_4[V^VO(O_2)(R,S\text{-mal})_2]\cdot 4H_2O$  and  $K_2[V^VO(O_2)(R,S\text{-Hmal})_2]\cdot 2H_2O$ ,<sup>23</sup> the oxidation states of V cations in **3B** are +4, as will be discussed below. A noteworthy structural feature is that  $atrz^-$  in **3** behaves as a 3-connected node, which is different from  $Hatrz$  and  $trz^-$ , adopting the  $\mu_{1,2}$ -bridging mode in **1** and **2**. However, the former coordination mode is the most common in metal azolate frameworks (MAFs).<sup>24</sup> The uncoordinated N atoms in **2** or NH<sub>2</sub> groups in **3** of two face-to-face triazoles present a staggered arrangement, which is ascribed to the steric hindrance and electrostatic repulsion between the same atoms. The V– $\mu_2$ –O distances in  $\Delta_{R-1}$  and  $\Lambda_{S-1}$  are 1.802(2) and 1.806(2) Å, respectively, while the V– $\mu_2$ –O distances in **2** and **3A** lie in the range of 1.730(2)–1.864(2) Å and 1.753(5)–1.837(5) Å, respectively. These are structural evidences for the electron delocalizations in  $\{V_6^{III/IV}O_5\}$  cores of **1**–**3A**. The V–V distances between adjacent V atoms vary from 3.362(2) to 3.642(3) Å, indicating weak intermetallic interactions in **1**–**3A**. Furthermore, the two parallel triazole rings in each molecule interact by intramolecular  $\pi\cdots\pi$  stacking, with the centroid to centroid distances of 3.508(6), 3.640(2), and 3.381(5) Å for **1**–**3**, respectively. Meanwhile, the dihedral angle between two triazole rings coordinated with the same V atoms in  $\Delta_{R-1}$  is 21.70°, while the values for **2** and **3** range from 2.23–5.52 to 13.36–16.33°, respectively. These results suggest that the values of dihedral angles may affect the formation of hydrogen bonds between adjacent molecules. That is, the bridging triazole ligands in the  $\{V^{III/IV}_6O_5\}$  core in **1** adopt a propeller-like twist to accommodate the hydrogen bonding requirements for  $N-H\cdots O=C$ . This arrangement reduces the symmetry of the molecule to crystallize in the chiral space group.<sup>25</sup> Detailed crystallographic data and selected bond distances and angles for **1**–**3** are summarized in Tables S1 and S2.

An interesting observation in **1** is the spontaneous resolution of enantiomers upon crystallization, where  $\Delta_{R-1}$  exhibits mirror symmetry with  $\Lambda_{S-1}$ . Since the unit-cell parameters, related bond distances, and angles of  $\Delta_{R-1}$  and  $\Lambda_{S-1}$  are almost identical, the hierarchical structure in  $\Delta_{R-1}$  is taken for discussion as a representative to gain a better insight into the

assembly logic of **1**. As shown in Figure 4 and Table S3, adjacent  $\Delta_{R-1}$  clusters display helical turns. They are held together through strong intermolecular interactions of hydrogen bonds, which are between 4-positioned N-atoms from 3,5-diamino-1,2,4-triazoles and  $\beta$ -carboxy oxygens from *R*-malates [such as  $N3-H\cdots O2^a$  2.635(9) Å,  $a(y, x, 1 - z)$ ]. They generate a unique left-handed helical chain running along the crystallographic 6<sub>3</sub>-screw axis ( $c$ -axis) with a pitch of 49.1 Å. As a result, the triple helical chains associate further in parallel to self-assemble into a supramolecular nanotube with a large exterior wall diameter of 34.0 Å and an interior channel diameter of 13.6 Å. The chiral space group means that all triple helical chains exist in the same chirality, showing that hydrogen bonds and helical structures should be closely related to chirality spontaneous resolution upon crystallization.<sup>26–28</sup> These supramolecular nanotubes are further joined together through intermolecular hydrogen bonds ( $N-H\cdots O$ ), forming a chiral POV-based supramolecular open-framework. Moreover, the amino groups in 3,5-diamino-1,2,4-triazoles and  $\alpha$ -carboxy groups in malates are all pointed toward the screw axis, thereby leading to the nanotubular channels with high polarizability. The total solvent-accessible volume for  $\Delta_{R-1}$  is calculated to be 2365.3 Å<sup>3</sup>, which takes up about 44.2% of the total crystal volume through PLATON application software.<sup>29</sup> From the topological point of view, if each  $\Delta_{R-1}$  monomer is taken as a node, the whole network can be simplified as a 3-connected 3D network with the Schläfli symbol of {6<sup>3</sup>} (Figure S2). In contrast to homochiral packing modes in  $\Delta_{R-1}$  and  $\Lambda_{S-1}$ , the opposite handedness of  $[V_5^{III}V_4^{IV}O_5(R\text{-mal})_6(3\text{-trz})_6]^{7-}$  and  $[V_5^{III}V_4^{IV}O_5(S\text{-mal})_6(3\text{-trz})_6]^{7-}$  for **2**,  $[V_3^{III}V_1^{IV}O_{11}(R\text{-mal})_{12}(atrz)_6]^{11-}$  and  $[V_3^{III}V_1^{IV}O_{11}(S\text{-mal})_{12}(atrz)_6]^{11-}$  for **3** are mainly linked by electrostatic interactions generated by potassium ions. They coexist in the unit cell with equal stoichiometry, canceling their chirality with the final racemic crystals (Figure S3). An irregular microchannel can also be found in **3** when viewed along the  $a$ -axis with lengths of 14.0 Å long and 4.1 Å wide, with the charge-balancing K<sup>+</sup> cations and guest water molecules located in the discrete channels (Figure S4). Factors responsible for spontaneous resolution may include but are not limited to the following points. The intermolecular hydrogen bonds with directionality [ $N3\cdots O2^a$  2.635(9) Å,  $a(y, x, 1 - z)$ ] in **1** are stronger than those in **2** [ $C13\cdots O14^a$  3.132(2) Å,  $a(x, 1 - y, 1/2 + z)$ ] and **3** [ $N8\cdots O56^a$  2.980(2) Å,  $a(-x, 2 - y, 1 - z)$ ], allowing **1** to be identified with the same configuration. Second, the supramolecular helices driven by hydrogen bonds associate in

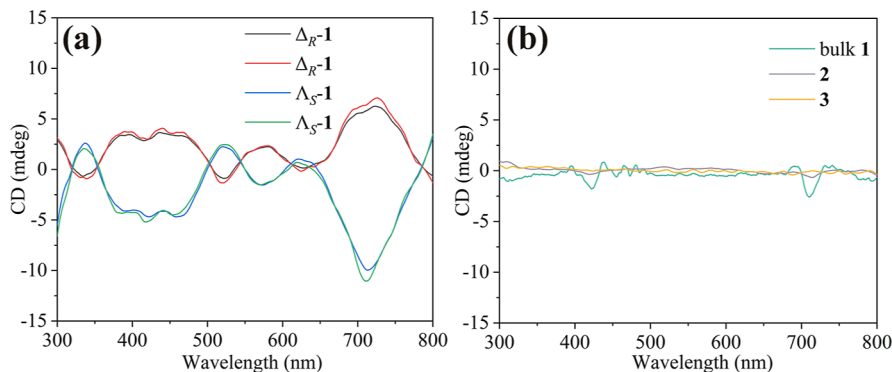


**Figure 5.** Solid-state CD spectra for (a) single crystals of  $\Delta_R\text{-1}$  and  $\Lambda_S\text{-1}$ , (b) bulk sample **1**, and single crystals of **2** and **3**.

parallel to each other, thus ensuring self-recognition.<sup>30</sup> Here, fine-tuning of secondary ligands induces dramatic supramolecular chirality, and the hydrogen bonding interactions between the molecules can be employed to selectively separate the cluster enantiomers, resulting in conglomerate crystals.<sup>31,32</sup>

**BVS Calculations.** As listed in Table S4, bond valence sum calculations show that the oxidation states of V1 in  $\Delta_R\text{-1}$ ,  $\Lambda_S\text{-1}$ , **2**, and **3A** are 3.080, 2.914, 2.878, and 2.981, respectively, revealing that the bicapped V atoms in **1–3A** are assigned as V<sup>III</sup> states unequivocally. This V<sup>III</sup> state is congruent with that of FeV-co, which has been revealed by X-ray absorption spectroscopy (XAS), density functional theory (DFT), and BVS calculations.<sup>9,33</sup> The BVS outcomes also give the oxidation states of 4.021 for V4 in **2**, 3.891, 3.877, 3.954, and 3.806 for V4–V7 in **3A**, which are clearly identified as V<sup>IV</sup> states. However, the valencies of the V2 atom in **1** and V2 and V3 atoms in **2** and **3** in {V<sub>6</sub>O<sub>5</sub>} cores are ambiguous between +3 and +4, indicating that these vanadium centers have some degree of mixed-valence states with strong electron delocalization, which is similar to previously reported mixed-valent vanadium clusters.<sup>14,34</sup> BVS calculations for  $\mu_2\text{-O}$  and  $\mu_3\text{-O}$  atoms in **1–3** show that they are all in O<sup>2-</sup> states (Table S5). Charge balance considerations indicate the assignments of the six vanadium centers in {V<sub>6</sub>O<sub>5</sub>} cores are V<sup>III</sup><sub>2</sub>V<sup>IV</sup><sub>4</sub> in **1**, V<sup>III</sup><sub>3</sub>V<sup>IV</sup><sub>3</sub> in **2**, and V<sup>III</sup><sub>1</sub>V<sup>IV</sup><sub>5</sub> in **3A**, respectively. That is, the formal oxidation states of eight V ions are calculated as V<sup>III</sup><sub>4</sub>V<sup>IV</sup><sub>4</sub> in **1**, V<sup>III</sup><sub>5</sub>V<sup>IV</sup><sub>3</sub> in **2**, and V<sup>III</sup><sub>3</sub>V<sup>IV</sup><sub>5</sub> in **3A**, which suggests that the oxidation states of vanadium ions can be altered by fine-tuning auxiliary ligands. In addition, all the vanadium centers in **3B** are assigned to +4 oxidation states, in accordance with structural analysis with V=O groups.

**Fourier Transform Infrared Spectra and Circular Dichroism Spectra.** The FTIR spectra of samples **1–3** exhibit several absorptions for various vibrationally active groups, as illustrated in Figure S5. Strong broad absorptions around 3440 cm<sup>-1</sup> are assigned to  $\nu(\text{O-H})$  of crystallized water molecules in **1–3**. The peak around 3341 cm<sup>-1</sup> in **1** and **3** is assigned to stretching vibrations of NH<sub>2</sub>. Specifically, the antisymmetric stretching vibrations  $\nu_{\text{as}}(\text{COO}^-)$  of carboxy groups are present at 1662 cm<sup>-1</sup> for **1**, 1648 cm<sup>-1</sup> for **2**, and 1646 cm<sup>-1</sup> for **3**, respectively, and the corresponding symmetric stretching vibrations  $\nu_s(\text{COO}^-)$  are observed around 1371 cm<sup>-1</sup> for **1**, 1375 cm<sup>-1</sup> for **2**, and 1397 cm<sup>-1</sup> for **3**, respectively. The asymmetric and symmetric stretching vibrations with splitting values  $\Delta[\nu_{\text{as}}(\text{COO}^-) - \nu_s(\text{COO}^-)]$  are greater than 200 cm<sup>-1</sup>, indicating that the carboxy groups in the molecules were either free or coordinated to the vanadium ion in a monodentate fashion.<sup>35,36</sup> The latter

deduction is supported by X-ray structural analyses of **1–3**. The carboxy absorptions shifted to lower frequencies with respect to those of free malic acid (1701 and 1442 cm<sup>-1</sup> derived from the Spectral Database for Organic Compounds), indicative of the change in the vibrational status of the ligand upon coordination to the vanadium cation.<sup>23</sup> The distinct bands observed in 593–895 cm<sup>-1</sup> for **1**, 601–884 cm<sup>-1</sup> for **2**, and 591–894 cm<sup>-1</sup> for **3** are attributed to the V–O–V stretching vibrations, while the strong V=O stretching vibration in **3B** occurs at 958 cm<sup>-1</sup>.

To confirm the resolution of enantiomers  $\Delta_R\text{-1}$  and  $\Lambda_S\text{-1}$ , both single-crystal X-ray diffraction analyses and solid-state circular dichroism spectra were further recorded. 10 single crystals of **1** were randomly selected from one batch and analyzed through single-crystal X-ray diffraction. Six of the crystals are  $\Lambda_S\text{-1}$ , while the other four are shown to be  $\Delta_R\text{-1}$ . Based upon the structural analyses, solid-state CD spectra of four large crystals mixed with transparent KBr pellets were further measured to examine the chiroptical activities of  $\Delta_R\text{-1}$  and  $\Lambda_S\text{-1}$ , respectively. As recorded in Figure 5a, strong circular dichroism signals with positive and negative Cotton effects were observed for  $\Delta_R\text{-1}$  and  $\Lambda_S\text{-1}$  in the wavelength range of 300–800 nm. As envisioned, the CD spectra exhibit mirror image inversions, confirming their chiral enantiomeric relationship. The optical activity of  $\Delta_R\text{-1}$  and  $\Lambda_S\text{-1}$  differs noticeably from that of R- and S-malic acids, which show only one Cotton effect around 218 nm, with silent CD signals in the visible regions.<sup>37</sup> In contrast,  $\Delta_R\text{-1}$  and  $\Lambda_S\text{-1}$  show several strong Cotton effects higher above 300 nm, which can be generated by ligand-to-metal charge transfer (300–500 nm) and the d-d transition of the V centers (500–800 nm). It should be noted that bulk sample **1** was also CD active in Figure 5b. The result indicates that an imbalanced formation of enantiomeric crystals occurs upon crystallization, which is preferential for the  $\Lambda_S\text{-1}$  isomer. However, no CD signal was observed for crystals **2** and **3**, indicating that **2** and **3** are racemic products.

**Thermogravimetric and Powder X-ray Diffraction Analyses.** Thermogravimetric analyses were performed to assess the thermal stabilities of **1–3** under an N<sub>2</sub> atmosphere. As shown in Figure S6a–c, **1–3** exhibited analogous weight-loss behavior but with different temperature ranges. The initial total weight losses of 21.8% at 86 °C for **1**, 12.3% at 66 °C for **2**, and 19.5% at 78 °C for **3** are ascribed to the removal of the guest and surface water molecules, respectively. Additional steps were observed in the ensuing thermal process up to 338, 382, and 260 °C for **1–3**, respectively, corresponding to the decompositions of the organic moiety bound to V ions and the collapse of the lattice structures, respectively. A TGA study was

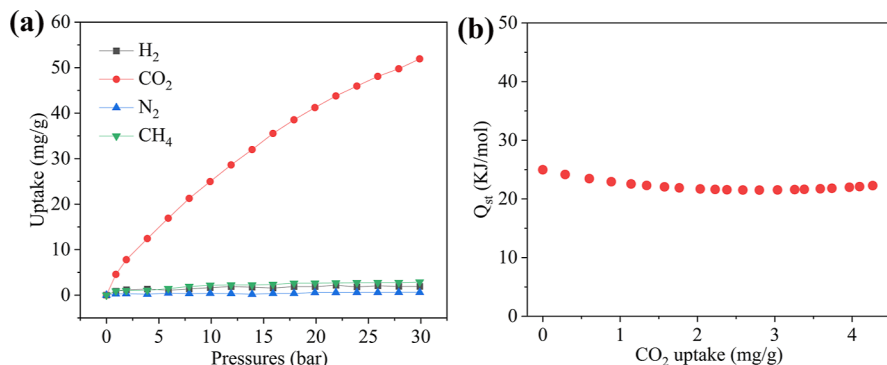


**Figure 6.** (a)  $\text{H}_2$ ,  $\text{CO}_2$ ,  $\text{N}_2$ , and  $\text{CH}_4$  adsorption isotherms of **1** at 25 °C, respectively. (b) Isosteric heats of  $\text{CO}_2$  adsorption ( $Q_{\text{st}}$ ) for **1**.

also conducted on the activated sample **1**. A slight weight loss around 100 °C (4.3%) can be observed, which is assigned to the moisture absorbed by the activated sample exposed to the air before the TGA test. The framework was then thermally stable up to 200 °C (Figure S6d). This result indicates that activated sample **1** possesses good thermal stability.

Powder X-ray diffractions were used to verify the phase purities of bulk samples **1–3**. As shown in Figure S7, the measured diffraction peaks match well with their simulated data, confirming their good crystallinities and high phase purities. Furthermore, no obvious change was observed in main diffraction peaks after gas adsorptions, indicating that sample **1** can retain its crystallinity and framework structure after adsorption tests.

**Gas Adsorptions.** To examine the porous nature of bulk sample **1**, a nitrogen adsorption–desorption isotherm was recorded at a temperature of 77 K. As displayed in Figure S8, the  $\text{N}_2$  isotherm showed very low nitrogen sorption. Although the channel size (13.6 Å) of **1** is noticeably larger than that of  $\text{N}_2$  (3.6 Å), only a tiny quantity of  $\text{N}_2$  adsorption can be ascribed to the availability of 1D channels along the *c*-axis, with no extra effective channels along the *a*- or *b*-axes. Actually, similar phenomena with no or very low  $\text{N}_2$  adsorption at 77 K for polyoxometalate (POM)-based porous materials have also been found in the literatures.<sup>38,39</sup> These can be attributed to the fact that the porous POM structures are constructed from hydrophilic POM moieties. However, given the abundant active sites in 1D channels, the adsorption characteristics of small-molecule gases like  $\text{CO}_2$ ,  $\text{H}_2$ ,  $\text{N}_2$ , and  $\text{CH}_4$  were further explored at various pressures. As shown in Figure 6a, sample **1** exhibited remarkably selective capture for  $\text{CO}_2$ , but little or no response to  $\text{H}_2$ ,  $\text{N}_2$ , and  $\text{CH}_4$ . This phenomenon can be associated with the interactions between gas molecules and pore surfaces. The  $\text{CO}_2$  adsorption isotherm of **1** satisfies the typical type I Langmuir adsorption model, which shows a rapid increase in the adsorption uptake with the increase in pressure, followed by a gentle gradient in the uptake until the saturation pressure. Upon pressure augmentation, the quantities of adsorbed  $\text{CO}_2$  for **1** gradually increased with 4.56, 24.96, and 41.21 mg·g<sup>-1</sup> at 0.9, 9.9, and 19.9 bar, respectively, and exhibited a maximum  $\text{CO}_2$  uptake of 51.93 mg·g<sup>-1</sup> at 29.9 bar. This enhanced affinity for  $\text{CO}_2$  of **1** arises mainly from the channel rich in  $\text{NH}_2$ -functionalized sites, which can generate a strong electrostatic interaction to facilitate selective  $\text{CO}_2$  capture.<sup>40,41</sup> Especially, pairs of N atoms [such as  $\text{N}^{\text{S}}\cdots\text{N}^{\text{S}}$  5.601 Å,  $a(y, x, 1 - z)$ ] from amino groups of adjacent molecules in channels can act as molecular claws whose  $\text{CO}_2$  dynamic sorption behavior has been confirmed by single-

crystal X-ray diffraction.<sup>42</sup> Also, the rich electrons from carboxyl groups and triazoles endow the channels with high polarizability,<sup>43</sup> and strong quadrupole–quadrupole interactions occur between  $\text{CO}_2$  and channels, resulting in the preferential affinity for  $\text{CO}_2$  over other gases.<sup>44–46</sup> Since the isosteric heat of adsorption ( $Q_{\text{st}}$ ) is commonly used to evaluate the strength of the host–guest interaction between the framework and  $\text{CO}_2$ , single-component adsorption performances of **1** for  $\text{CO}_2$  at 25 and 15 °C were also recorded at 1 bar (Figure S9). Based on the Clausius–Clapeyron equation and Virial fitting method, the  $Q_{\text{st}}$  value of  $\text{CO}_2$  at zero coverage is calculated to be 24.83 kJ·mol<sup>-1</sup> for **1** (Figure 6b), which is slightly higher than that functionalized with N-heterocycles such as MAF-26 (23.3 kJ·mol<sup>-1</sup>).<sup>47</sup> and exposed cations such as Cu-BTTri (21.0 kJ·mol<sup>-1</sup>).<sup>48</sup> We further predicted the adsorption selectivities toward  $\text{CO}_2/\text{CH}_4$  (v/v = 50/50) mixed gases according to ideal adsorbed solution theory (IAST),<sup>49</sup> where the single-component adsorption isotherms were fitted by the single-site Langmuir–Freundlich model. As shown in Figure S10, the selectivity for  $\text{CO}_2$  over  $\text{CH}_4$  was calculated to be 9.44 under standard atmospheric pressure for **1**, similar to that of  $[\text{Zn}_2(\text{atz})_2(\text{ipa})]$  (9.60,  $\text{H}_2\text{ipa}$  = isophthalic acid),<sup>50</sup> but higher than that of InOF-15 (7.7),<sup>51</sup> ZJNU-10 (7.6),<sup>52</sup>  $[\text{Zn}_{24}(\text{BDPO})_{12}(\text{DMF})_{12}] \cdot 6\text{DMF} \cdot 52\text{H}_2\text{O}$  (7.0),<sup>53</sup> and MOF-205-OBn (2.7).<sup>54</sup> These results support the positive effect of amino groups for  $\text{CO}_2$  capture, demonstrating that sample **1** is favorable for the selective separation of  $\text{CO}_2$  over  $\text{CH}_4$ .

Comparisons of the adsorbed  $\text{CO}_2$  quantity for **1** with other porous polyoxometalates are listed in Table S6. Sample **1** exhibits good  $\text{CO}_2$  adsorption capacity at atmospheric pressure, when it compared with other microporous polyoxometalate frameworks like  $\text{Na}_3[\text{Mo}^{\text{V}}_6\text{O}_6(\mu_2-\text{O})_9(\text{Htrz})_3(\text{trz})_3] \cdot 7.5\text{H}_2\text{O}$ ,<sup>55</sup>  $[\text{Cu}(\text{en})_2]_6\{[\text{Cu}(\text{en})_2] @ \{[\text{Cu}_2(\text{trz})_2(\text{en})_2\}_6[\text{H}_{10}\text{Nb}_{68}\text{O}_{188}]\},$ <sup>38</sup>  $\{[\text{Cu}(\text{en})_2] @ \{[\text{Cu}_2(\text{en})_2(\text{trz})_2\}_6(\text{Nb}_{68}\text{O}_{188})\}\}^{22-}$ ,<sup>38</sup> and  $\text{K}_4 @ \{[\text{Cu}_2(\text{O}\text{H})_7(\text{H}_2\text{O})_2(\text{en})_8(\text{trz})_2\}_1 \cdot [\text{H}_2\text{Nb}_{24}\text{O}_{69}(\text{H}_2\text{O})_3\}_4\}^{30-38}$ . The quantity of adsorbed  $\text{CO}_2$  adsorption in **1** is lower than mesoporous polyoxometalates framework SUT-7<sup>56</sup> at low pressure, which is ascribed to the microporous structure. Although the  $\text{CO}_2$  adsorption capacity for **1** is modest at room temperature and atmospheric conditions, **1** may be useful for  $\text{CO}_2$  adsorption at high pressure.

**Chiral Interface Recognition.** Given the homochiral nature of the internal surface in  $\Delta_{\text{R}}\text{-1}$ , enantioselective sorption is of great interest. We have investigated the enantioselective recognition of  $\Delta_{\text{R}}\text{-1}$  for small chiral molecules. To probe the chiral interface recognition of  $\Delta_{\text{R}}\text{-1}$  for small organic molecules

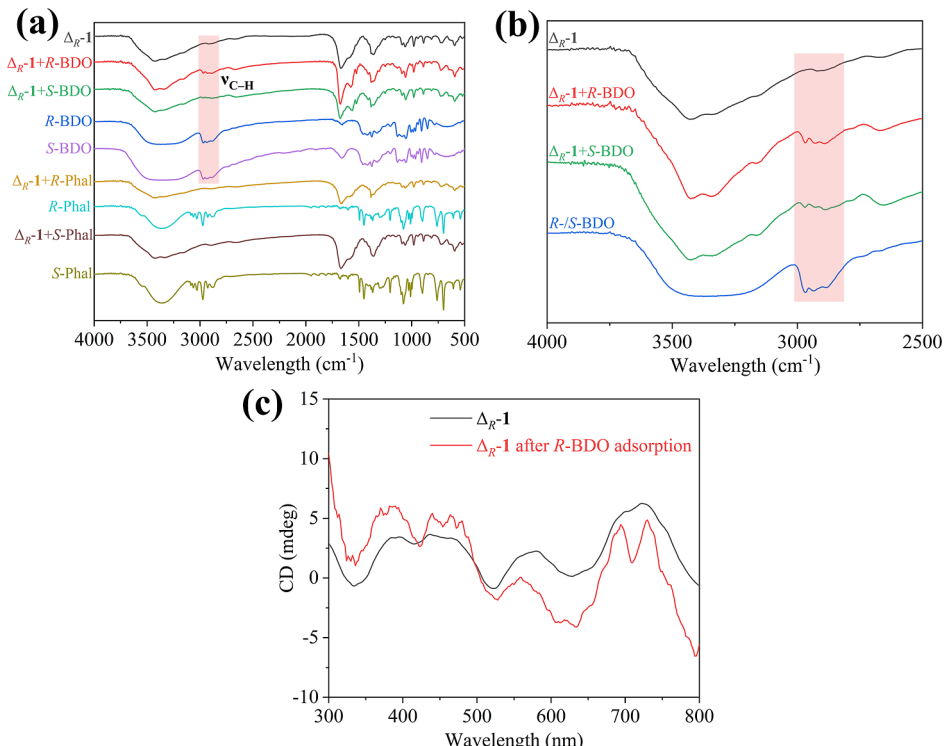


**Figure 7.** (a) FTIR spectra of  $\Delta_R\text{-1}$ , R-/S-BDO, R-/S-Phal, and  $\Delta_R\text{-1}$  after R-/S-BDO and R-/S-Phal adsorption, respectively. (b) FTIR spectra with local amplification regions of  $\Delta_R\text{-1}$ , R-/S-BDO, and  $\Delta_R\text{-1}$  after R-/S-BDO adsorptions, respectively. (c) Solid-state CD spectra for  $\Delta_R\text{-1}$  before and after R-BDO adsorptions.

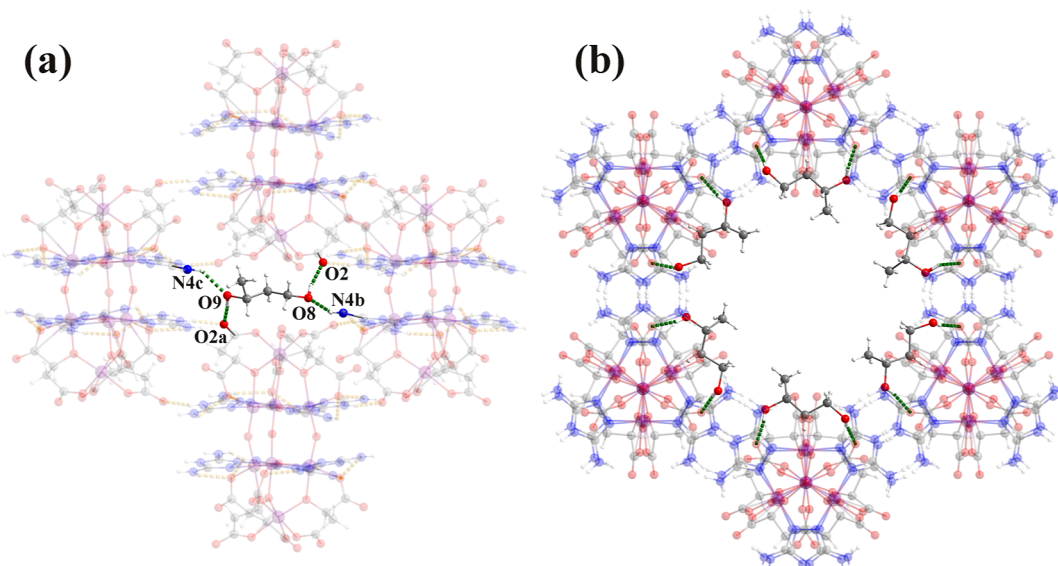


**Figure 8.** Structure of the host–guest complex  $\Delta_R\text{-1}\cdot\text{R-BDO}$  viewed along the (a) *b*-axis and (b) *c*-axis. The host–guest interactions are shown in green dotted lines.

in the chiral channels, we have obtained homochiral  $\Delta_R\text{-1}$  with chiral ligand *R*-malic acid. Prior to the chiral interface recognition studies, the FTIR spectrum of  $\Delta_R\text{-1}$  was investigated after ethanol treatment for 24 h at room temperature. As shown in Figure S11, the result revealed that  $\Delta_R\text{-1}$  did not change before and after the ethanol treatment, exhibiting good structural stability in ethanol. In the chiral interface recognition experiments,  $\Delta_R\text{-1}$  was immersed in ethanol solutions of *R*-1,3-butanediol (R-BDO), *S*-1,3-butanediol (S-BDO), *R*-1-phenylethanol (*R*-Phal), or *S*-1-

phenylethanol (*S*-Phal) for 24 h, respectively. After that, the collected drying samples were further analyzed by FTIR spectra. As shown in Figure 7a,b, there are additional peaks detected in the range of 2800–3000 cm<sup>-1</sup> in  $\Delta_R\text{-1}$  after R-BDO (red curve) and S-BDO (green curve, very weak) adsorptions, while none in pure  $\Delta_R\text{-1}$  (black curve) or *R*-/S-Phal adsorptions (orange and brown curves). The new peaks observed at 2967, 2928, and 2890 cm<sup>-1</sup> correspond to the characteristic vibrational bands of C–H stretching, referring to the IR spectra of free *R*-/S-BDO (blue and violet curves),

suggesting that the molecule *R*-BDO adsorbed preferentially on the channels over *S*-BDO. Due to the stereochemical effects in the chiral channels, chiral interface recognition generally stems from a specific host–guest interaction, which might generate subtle changes in optical spectra.<sup>57,58</sup> Thus, the CD spectrum was further performed to characterize  $\Delta_R\text{-1}$  after *R*-BDO adsorption. Compared with pure  $\Delta_R\text{-1}$ , the red curve for  $\Delta_R\text{-1}$  after *R*-BDO adsorption shows a slight blue shift observed in Figure 7c, suggesting that  $\Delta_R\text{-1}$  has a good affinity to interact with *R*-BDO. As mentioned above, the nanotubular channels with a high polarizability of  $\Delta_R\text{-1}$  might generate strong intermolecular hydrogen bonding and interaction between channels and *R*-1,3-butanediol. Fortunately, we have successfully isolated a host–guest crystal  $\Delta_R\text{-1}\cdot 3(R\text{-BDO})$  by soaking the as-synthesized  $\Delta_R\text{-1}$  crystal in *R,S*-BDO for 12 h and further examined with single-crystal X-ray diffraction analysis. As shown in Figure 8, X-ray structural analysis revealed that the guest molecule *R*-BDO occupies the chiral channels of  $\Delta_R\text{-1}$ , where the inclusion of the guest molecules did not result in any significant distortion in the original host structure, with a slight increase of the unit cell volume ( $\Delta = 135 \text{ \AA}^3$ , Table S1). The alcohol group of each *R*-BDO interacts with four  $\Delta_R\text{-1}$  molecules through strong hydrogen bonding with  $\beta$ -carboxy groups of *R*-mal and amino groups of Hdatrz [O8…O2 2.723(2) Å, O9…O2<sup>a</sup> 2.687(2) Å, O8…N4<sup>b</sup> 2.874(2) Å, O9…N4<sup>c</sup> 2.846(2) Å,  $a = 1 + y - x$ ,  $y, 1/2 - z$ ,  $b = 1 - x, 1 - y, -1/2 + z$ ,  $c = 1 - y + x, 1 - y, 1 - z$ ]. That is, the  $\beta$ -carboxy groups of malates in channels can serve as molecular claws for chiral interface recognitions for *R*-BDO. It is interesting to note that there are six *R*-BDO molecules in the channel, reducing its diameter from 13.6 to 9.0 Å. To further evaluate the enantioselective separation of  $\Delta_R\text{-1}$  for *R,S*-BDO, the enantiomeric excess (ee) value was measured by applying a gas chromatography (GC) technique (see Supporting Information for details). As shown in Table 1 and Figure

**Table 1. Enantioselective Separation for Racemates at Room Temperature**

| host                | guest                        | ee (%) |
|---------------------|------------------------------|--------|
| $\Delta_R\text{-1}$ | <i>R,S</i> -BDO <sup>a</sup> | 16     |

<sup>a</sup>The enantiomeric excess (ee) =  $(R - S)/(R + S) \times 100$  for *R,S*-BDO was determined for the trifluoroacetic anhydride derivatives on a Chiralsil-DEX CB.

**S12**,  $\Delta_R\text{-1}$  can adsorb more *R*-BDO from *R,S*-BDO, with an ee value of 16%, close to that of  $[\text{Ni}_2(\text{l-asp})_2(\text{bipy})]$  (17.93%).<sup>59</sup> The control experiment using *R*-malic acid did not show any chiral recognition for *R*-/S-BDO, suggesting a critical role for chiral channels. These results indicate that the chiral channel of  $\Delta_R\text{-1}$  is more favorable for the adsorption of *R*-1,3-butanediol, which reflects that  $\Delta_R\text{-1}$  is capable of performing chiral interface recognition.

## CONCLUSIONS

In summary, we have obtained a pair of chiral cage-like polyoxovanadates(III/IV) enantiomers  $\Delta_R\text{-1}$  and  $\Delta_S\text{-1}$ , together with their two heterochiral complexes 2 and 3 through dual-ligand synthetic strategies, where an interesting in situ decarboxylation reaction occurs in the formation of 3-amino-1,2,4-triazole. All of them are constructed from a bicapped-triangular-prismatic  $\{\text{V}_8\text{O}_5(\text{mal})_6\}$  building block with five- and six-membered rings chelated by malates. The local

chelation environment with a  $\Delta_R$ -configuration shows a little similarity with that in FeV-co. The spontaneous resolution of enantiomers  $\Delta_R\text{-1}$  and  $\Delta_S\text{-1}$  happens as unique triple helical supramolecular structures via hydrogen bonding interactions. The chiral POV-based supramolecular open-framework 1 decorated with amine-functionalized groups on the pore surfaces can attract CO<sub>2</sub> more favorably with little or no adsorption for gases N<sub>2</sub>, CH<sub>4</sub>, and H<sub>2</sub>. Importantly, homochiral framework  $\Delta_R\text{-1}$  exhibits chiral interface recognition for *R*-1,3-butanediol through host–guest interactions between the porous framework and guest molecules, which has been confirmed by single-crystal X-ray diffraction and GC analysis. Six chiral *R*-1,3-butanediols have been recognized inside the nanotubular channel (13.6 Å) constructed by the skeleton of  $\Delta_R\text{-1}$ . Thus,  $\Delta_R\text{-1}$  looks promising for chiral interface recognition for small organic molecules.

## ASSOCIATED CONTENT

### Supporting Information

The Supporting Information is available free of charge at <https://pubs.acs.org/doi/10.1021/acsami.3c06493>.

Experimental details, perspective views, IR spectra, TGA curves, PXRD analyses, N<sub>2</sub> adsorption–desorption isotherms, CO<sub>2</sub> and CH<sub>4</sub> adsorption isotherms, IAST selectivity, GC analyses, detailed crystallographic data, selected bond distances and angles, hydrogen bonds, and BVS calculations for 1–3 (PDF)

## Accession Codes

CCDC 2223598–2223601 and 2259266 contain the supplementary crystallographic data for this paper. These data can be obtained free of charge from The Cambridge Crystallographic Data Centre via [www.ccdc.cam.ac.uk/data\\_request/cif](http://www.ccdc.cam.ac.uk/data_request/cif).

## AUTHOR INFORMATION

### Corresponding Author

Zhao-Hui Zhou – State Key Laboratory for Physical Chemistry of Solid Surfaces and College of Chemistry and Chemical Engineering, Xiamen University, Xiamen 361005, China;  [orcid.org/0000-0001-7271-7009](https://orcid.org/0000-0001-7271-7009); Phone: +86 592 2184531; Email: [zhzhou@xmu.edu.cn](mailto:zhzhou@xmu.edu.cn); Fax: +86 592 2183047

### Author

Zhen-Lang Xie – State Key Laboratory for Physical Chemistry of Solid Surfaces and College of Chemistry and Chemical Engineering, Xiamen University, Xiamen 361005, China;  [orcid.org/0000-0002-8558-7642](https://orcid.org/0000-0002-8558-7642)

Complete contact information is available at: <https://pubs.acs.org/10.1021/acsami.3c06493>

## Notes

The authors declare no competing financial interest.

## ACKNOWLEDGMENTS

We thank the National Natural Science Foundation of China (22179110) for the generous financial support. We acknowledge Professor Y.-Y. Li, Ms. R.-Y. Huang, and Dr. H. Xu for their assistances with GC and CD spectra measurements and single-crystal X-ray diffraction analyses, respectively.

## ■ REFERENCES

- (1) Ma, W.; Xu, L. G.; de Moura, A. F.; Wu, X.; Kuang, H.; Xu, C.; Kotov, N. A.; Kotov, N. A. Chiral Inorganic Nanostructures. *Chem. Rev.* **2017**, *117*, 8041–8093.
- (2) Jędrzejewska, H.; Szumna, A. Making a Right or Left Choice: Chiral Self-Sorting as a Tool for the Formation of Discrete Complex Structures. *Chem. Rev.* **2017**, *117*, 4863–4899.
- (3) Gu, Z. G.; Zhan, C. H.; Zhang, J.; Bu, X. H. Chiral Chemistry of Metal-Camphorate Frameworks. *Chem. Soc. Rev.* **2016**, *45*, 3122–3144.
- (4) Liu, M. H.; Zhang, L.; Wang, T. Y. Supramolecular Chirality in Self-Assembled Systems. *Chem. Rev.* **2015**, *115*, 7304–7397.
- (5) Sippel, D.; Einsle, O. The Structure of Vanadium Nitrogenase Reveals an Unusual Bridging Ligand. *Nat. Chem. Biol.* **2017**, *13*, 956–960.
- (6) Jasniewski, A. J.; Lee, C. C.; Ribbe, M. W.; Hu, Y. L. Reactivity, Mechanism, and Assembly of the Alternative Nitrogenases. *Chem. Rev.* **2020**, *120*, 5107–5157.
- (7) Einsle, O.; Rees, D. C. Structural Enzymology of Nitrogenase Enzymes. *Chem. Rev.* **2020**, *120*, 4969–5004.
- (8) Chen, C. Y.; Chen, M. L.; Chen, H. B.; Wang, H.; Cramer, S. P.; Zhou, Z. H. A-Hydroxy Coordination of Mononuclear Vanadyl Citrate, Malate and S-Citramalate with N-Heterocycle Ligand, Implying a New Protonation Pathway of Iron-Vanadium Cofactor in Nitrogenase. *J. Inorg. Biochem.* **2014**, *141*, 114–120.
- (9) Jin, W. T.; Yang, M.; Zhu, S. S.; Zhou, Z. H. Bond-Valence Analyses of the Crystal Structures of FeMo/V Cofactors in FeMo/V Proteins. *Acta Crystallogr., Sect. D: Struct. Biol.* **2020**, *76*, 428–437.
- (10) Sippel, D.; Rohde, M.; Netzer, J.; Trncik, C.; Gies, J.; Grunau, K.; Djurdjevic, I.; Decamps, L.; Andrade, S. L. A.; Einsle, O. A Bound Reaction Intermediate Sheds Light on the Mechanism of Nitrogenase. *Science* **2018**, *359*, 1484–1489.
- (11) Rohde, M.; Grunau, K.; Einsle, O. CO Binding to the FeV Cofactor of CO-Reducing Vanadium Nitrogenase at Atomic Resolution. *Angew. Chem., Int. Ed.* **2020**, *59*, 23626–23630.
- (12) Rohde, M.; Laun, K.; Zebger, I.; Stripp, S. T.; Einsle, O. Two Ligand-Binding Sites in CO-Reducing V Nitrogenase Reveal a General Mechanistic Principle. *Sci. Adv.* **2021**, *7*, No. eabg4474.
- (13) Newcomb, M. P.; Lee, C. C.; Tanifuchi, K.; Jasniewski, A. J.; Liedtke, J.; Ribbe, M. W.; Hu, Y. L. A V-Nitrogenase Variant Containing a Citrate-Substituted Cofactor. *Chembiochem* **2020**, *21*, 1742–1748.
- (14) Jin, W. T.; Yuan, C.; Deng, L.; An, D. L.; Zhou, Z. H. Isolated Mixed-Valence Iron Vanadium Malate and Its Metal Hydrates ( $M = Fe^{2+}, Cu^{2+}, Zn^{2+}$ ) with Reversible and Irreversible Adsorptions for Oxygen. *Inorg. Chem.* **2020**, *59*, 12768–12777.
- (15) Pasteur, L. Recherches Sur Les Relations Qui Peuvent Exister Entre La Forme Crystalline, La Composition Chimique Et Le Sens De La Polarisation Rotatoire. *Ann. Chim. Phys.* **1848**, *24*, 442.
- (16) Pérez García, L.; Amabilino, D. B. Spontaneous Resolution under Supramolecular Control. *Chem. Soc. Rev.* **2002**, *31*, 342–356.
- (17) Zhao, D.; Li, W.; Wen, R.; Lei, N.; Li, W.; Liu, X.; Zhang, X.; Fan, L. Eu(III)-Functionalized MOF-Based Dual-Emission Ratio-Metric Sensor Integrated with Logic Gate Operation for Efficient Detection of Hippuric Acid in Urine and Serum. *Inorg. Chem.* **2023**, *62*, 2715–2725.
- (18) Wang, F.; Zhao, D.; Li, W.; Zhang, H.; Li, B.; Hu, T.; Fan, L. Rod-Shaped Units Based Cobalt(II) Organic Framework as an Efficient Electrochemical Sensor for Uric Acid Detection in Serum. *Microchem. J.* **2023**, *185*, 108154.
- (19) Su, C. Y.; Goforth, A. M.; Smith, M. D.; Pellechia, P. J.; Zur Loye, H. C. Exceptionally Stable, Hollow Tubular Metal-Organic Architectures: Synthesis, Characterization, and Solid-State Transformation Study. *J. Am. Chem. Soc.* **2004**, *126*, 3576–3586.
- (20) Xiang, S.; Zhang, X.; Chen, H.; Li, Y.; Fan, W.; Huang, D. Copper(II) Facilitated Decarboxylation for the Construction of Pyridyl-Pyrazole Skeletons. *Inorg. Chem. Front.* **2019**, *6*, 2359–2364.
- (21) Li, J.; Brill, T. B. Spectroscopy of Hydrothermal Reactions 20: Experimental and DFT Computational Comparison of Decarboxylation of Dicarboxylic Acids Connected by Single, Double, and Triple Bonds. *J. Phys. Chem. A* **2002**, *106*, 9491–9498.
- (22) Li, D. P.; Zhou, X. H.; Liang, X. Q.; Li, C. H.; Chen, C.; Liu, J.; You, X. Z. Novel Structural Diversity of Triazolate-Based Coordination Polymers Generated Solvothermally with Anions. *Cryst. Growth Des.* **2010**, *10*, 2136–2145.
- (23) Kaliva, M.; Giannadaki, T.; Salifoglou, A.; Raptopoulou, C. P.; Terzis, A.; Tangoulis, V. pH-Dependent Investigations of Vanadium(V)-Peroxo-Malate Complexes from Aqueous Solutions. In Search of Biologically Relevant Vanadium(V)-Peroxo Species. *Inorg. Chem.* **2001**, *40*, 3711–3718.
- (24) Zhang, J. P.; Zhang, Y. B.; Lin, J. B.; Chen, X. M. Metal Azolate Frameworks: From Crystal Engineering to Functional Materials. *Chem. Rev.* **2012**, *112*, 1001–1033.
- (25) Lazarou, K. A.; Gonzalez-Nieves, K.; Chakraborty, I.; Raptis, R. G. Spontaneous Resolution by Crystallization of an Octanuclear Iron(III) Complex Using Only Racemic Reagents. *Angew. Chem., Int. Ed.* **2019**, *58*, 7324–7328.
- (26) Pérez-García, L.; Amabilino, D. B. Spontaneous Resolution, Whence and Whither: From Enantiomeric Solids to Chiral Liquid Crystals, Monolayers and Macro- and Supra-Molecular Polymers and Assemblies. *Chem. Soc. Rev.* **2007**, *36*, 941–967.
- (27) Stephenson, A.; Ward, M. D. A Triple Helix of Double Helicates: Three Hierarchical Levels of Self-Assembly in a Single Structure. *Chem. Commun.* **2012**, *48*, 3605–3607.
- (28) Liao, W. M.; Li, X. N.; Zeng, Q.; Zhong, Y. H.; Yin, Y. G.; He, J. Enantiomerism, Diastereomerism and Thermochromism in Two  $Cu_{7,4}$  Cluster-Based Coordination Polymers. *J. Mater. Chem. C* **2019**, *7*, 15136–15140.
- (29) Spek, A. L. Single-Crystal Structure Validation with the Program PLATON. *J. Appl. Crystallogr.* **2003**, *36*, 7–13.
- (30) Tang, X.; Chu, D.; Jiang, H.; Gong, W.; Jiang, C.; Cui, Y.; Liu, Y. Supramolecular Self-Assembly of Chiral Helical Tubular Polymers with Amplified Circularly Polarized Luminescence. *Mater. Chem. Front.* **2020**, *4*, 2772–2781.
- (31) Chen, Z. Y.; Hong, Q. L.; Zhang, H. X.; Zhang, J. Induction of Chirality in Boron Imidazolate Frameworks: The Structure-Directing Effects of Substituents. *Inorg. Chem.* **2022**, *61*, 6861–6868.
- (32) He, J.; Deng, C. L.; Sun, C. F.; Zhang, X. X.; Cui, Y.; Wu, S. H.; Luo, G. G. Controllable Spontaneous Resolution in Ultrasmall Cu-Ag Bimetallic Cluster Ion Pairs from Achiral Components. *Chem. Commun.* **2022**, *58*, 1577–1580.
- (33) Rees, J. A.; Bjornsson, R.; Kowalska, J. K.; Lima, F. A.; Schlesier, J.; Sippel, D.; Weyhermüller, T.; Einsle, O.; Kovacs, J. A.; DeBeer, S. Comparative Electronic Structures of Nitrogenase FeMoco and FeVco. *Dalton Trans.* **2017**, *46*, 2445–2455.
- (34) Keene, T. D.; D'Alessandro, D. M.; Kramer, K. W.; Price, J. R.; Price, D. J.; Decurtins, S.; Kepert, C. J.  $[V_{16}O_{38}(CN)]^{9-}$ : A Soluble Mixed-Valence Redox-Active Building Block with Strong Antiferromagnetic Coupling. *Inorg. Chem.* **2012**, *51*, 9192–9199.
- (35) Deacon, G. B.; Phillips, R. J. Relationships between the Carbon-Oxygen Stretching Frequencies of Carboxylato Complexes and the Type of Carboxylate Coordination. *Coord. Chem. Rev.* **1980**, *33*, 227–250.
- (36) Jin, W. T.; Zhou, Z. H. Novel Bidentate Oxovanadium(IV) Glycolate,  $\alpha$ -Hydroxybutyrate and Citrate with Terpyridine and Their Conversions to Nitrosyl Products. *J. Inorg. Biochem.* **2020**, *208*, 111086.
- (37) Wang, Y. L.; Zhao, J. W.; Zhang, Z.; Sun, J. J.; Li, X. Y.; Yang, B. F.; Yang, G. Y. Enantiomeric Polyoxometalates Based on Malate Chirality-Inducing Tetra-Zr(IV)-Substituted Keggin Dimeric Clusters. *Inorg. Chem.* **2019**, *58*, 4657–4664.
- (38) Zhu, Z. K.; Lin, Y. Y.; Yu, H.; Li, X. X.; Zheng, S. T. Inorganic-Organic Hybrid Polyoxoniobates: Polyoxoniobate Metal Complex Cage and Cage Framework. *Angew. Chem., Int. Ed.* **2019**, *58*, 16864–16868.
- (39) Zhou, E. L.; Qin, C.; Huang, P.; Wang, X. L.; Chen, W. C.; Shao, K. Z.; Su, Z. M. A Stable Polyoxometalate-Pillared Metal-

- Organic Framework for Proton-Conducting and Colorimetric Biosensing. *Chem.—Eur. J.* **2015**, *21*, 11894–11898.
- (40) Shi, Z.; Tao, Y.; Wu, J.; Zhang, C.; He, H.; Long, L.; Lee, Y.; Li, T.; Zhang, Y. B. Robust Metal-Triazolate Frameworks for CO<sub>2</sub> Capture from Flue Gas. *J. Am. Chem. Soc.* **2020**, *142*, 2750–2754.
- (41) Xie, Z. L.; An, D. L.; Weng, W. Z.; Zhou, Z. H. Successive Constructions of Regular Tetra-Hexa- and Octanuclear Microporous Polyoxovanadates(III) for Gas Adsorptions. *Dalton Trans.* **2022**, *51*, 11286–11294.
- (42) Liao, P. Q.; Zhou, D. D.; Zhu, A. X.; Jiang, L.; Lin, R. B.; Zhang, J. P.; Chen, X. M. Strong and Dynamic CO<sub>2</sub> Sorption in a Flexible Porous Framework Possessing Guest Chelating Claws. *J. Am. Chem. Soc.* **2012**, *134*, 17380–17383.
- (43) Sheng, D. H.; Zhang, Y.; Han, Y.; Xu, G.; Song, Q. X.; Hu, Y. P.; Liu, X. Y.; Shan, D. M.; Cheng, A. C. A Zinc(II) Metal-Organic Framework with High Affinity for CO<sub>2</sub> Based on Triazole and Tetrazolyl Benzene Carboxylic Acid. *CrystEngComm* **2019**, *21*, 3679–3685.
- (44) Sumida, K.; Rogow, D. L.; Mason, J. A.; McDonald, T. M.; Bloch, E. D.; Herm, Z. R.; Bae, T. H.; Long, J. R. Carbon Dioxide Capture in Metal-Organic Frameworks. *Chem. Rev.* **2012**, *112*, 724–781.
- (45) Chaemchuen, S.; Kabir, N. A.; Zhou, K.; Verpoort, F. Metal-Organic Frameworks for Upgrading Biogas via CO<sub>2</sub> Adsorption to Biogas Green Energy. *Chem. Soc. Rev.* **2013**, *42*, 9304–9332.
- (46) Gu, Y.; Zheng, J. J.; Otake, K. I.; Shivanna, M.; Sakaki, S.; Yoshino, H.; Ohba, M.; Kawaguchi, S.; Wang, Y.; Li, F.; et al. Host-Guest Interaction Modulation in Porous Coordination Polymers for Inverse Selective CO<sub>2</sub>/C<sub>2</sub>H<sub>2</sub> Separation. *Angew. Chem., Int. Ed.* **2021**, *60*, 11688–11694.
- (47) Lin, J. B.; Zhang, J. P.; Chen, X. M. Nonclassical Active Site for Enhanced Gas Sorption in Porous Coordination Polymer. *J. Am. Chem. Soc.* **2010**, *132*, 6654–6656.
- (48) Demessence, A.; D'Alessandro, D. M.; Foo, M. L.; Long, J. R. Strong CO<sub>2</sub> Binding in a Water-Stable, Triazolate-Bridged Metal-Organic Framework Functionalized with Ethylenediamine. *J. Am. Chem. Soc.* **2009**, *131*, 8784–8786.
- (49) Myers, A. L.; Prausnitz, J. M. Thermodynamics of Mixed-Gas Adsorption. *AIChE J.* **1965**, *11*, 121–127.
- (50) Chen, K. J.; Lin, R. B.; Liao, P. Q.; He, C. T.; Lin, J. B.; Xue, W.; Zhang, Y. B.; Zhang, J. P.; Chen, X. M. New Zn-Aminotriazolate-Dicarboxylate Frameworks: Synthesis, Structures, and Adsorption Properties. *Cryst. Growth Des.* **2013**, *13*, 2118–2123.
- (51) Qian, J. J.; Li, Q. P.; Liang, L. F.; Li, T. T.; Hu, Y.; Huang, S. M. A Microporous MOF with Open Metal Sites and Lewis Basic Sites for Selective CO<sub>2</sub> Capture. *Dalton Trans.* **2017**, *46*, 14102–14106.
- (52) Gao, X.; Xu, T.; Jiang, Z.; Yu, H.; Wang, Y.; He, Y. Rational Construction and Remarkable Gas Adsorption Properties of a HKUST-1-Like tbo-Type MOF Based on a Tetraisophthalate Linker. *Dalton Trans.* **2019**, *48*, 16793–16799.
- (53) He, H. M.; Zhang, D. Y.; Guo, F.; Sun, F. X. A Versatile Microporous Zinc(II) Metal-Organic Framework for Selective Gas Adsorption, Cooperative Catalysis, and Luminescent Sensing. *Inorg. Chem.* **2018**, *57*, 7314–7320.
- (54) Sim, J.; Yim, H.; Ko, N.; Choi, S. B.; Oh, Y.; Park, H. J.; Park, S.; Kim, J. Gas Adsorption Properties of Highly Porous Metal-Organic Frameworks Containing Functionalized Naphthalene Dicarboxylate Linkers. *Dalton Trans.* **2014**, *43*, 18017–18024.
- (55) Deng, L.; Dong, X.; Zhou, Z. H. Intrinsic Molybdenum-Based POMOFs with Impressive Gas Adsorptions and Photochromism. *Chem.—Eur. J.* **2021**, *27*, 9643–9653.
- (56) Chen, H.; Yu, Z. B.; Bacsik, Z.; Zhao, H. S.; Yao, Q. X.; Sun, J. L. Construction of Mesoporous Frameworks with Vanadoborate Clusters. *Angew. Chem., Int. Ed.* **2014**, *53*, 3608–3611.
- (57) Zhao, Y. W.; Wang, Y.; Zhang, X. M. Homochiral Mof as Circular Dichroism Sensor for Enantioselective Recognition on Nature and Chirality of Unmodified Amino Acids. *ACS Appl. Mater. Interfaces* **2017**, *9*, 20991–20999.
- (58) Weng, Z. Z.; Xu, H.; Zhang, W.; Zhuang, G. L.; Long, L. S.; Kong, X. J.; Zheng, L. S. Enantioselective Recognition and Separation of C<sub>2</sub> Symmetric Substances via Chiral Metal-Organic Frameworks. *ACS Appl. Mater. Interfaces* **2021**, *13*, 37412–37421.
- (59) Vaidyanathan, R.; Bradshaw, D.; Rebilly, J. N.; Barrio, J. P.; Gould, J. A.; Berry, N. G.; Rosseinsky, M. J. A Family of Nanoporous Materials Based on an Amino Acid Backbone. *Angew. Chem., Int. Ed.* **2006**, *45*, 6495–6499.